Nanoscale

PAPER

View Article Online
View Journal

Cite this: DOI: 10.1039/c4nr06180b

# On the mechanical and electronic properties of thiolated gold nanocrystals†

K. Smaali,‡[a] S. Desbief,‡[a] G. Foti,[b,c] T. Frederiksen,[c,d] D. Sanchez-Portal,[b,c] A. Arnau,[b,c,e] J. P. Nys,[a] P. Leclère,[f] D. Vuillaume[a] and N. Clément*[a]

Received 21st October 2014,
Accepted 2nd December 2014

DOI: 10.1039/c4nr06180b

www.rsc.org/nanoscale

We present a quantitative exploration, combining experiment and simulation, of the mechanical and electronic properties, as well as the modifications induced by an alkylthiolated coating, at the single nanoparticle (NP) level. We determined the response of the NPs to external pressure in a controlled manner using an atomic force microscope tip. We found a strong reduction in their Young's modulus, as compared to bulk gold, and a significant influence of strain on the electronic properties of the alkylthiolated NPs. Electron transport measurements of tiny molecular junctions (NP/alkylthiol/CAFM tip) show that the effective tunnelling barrier through the adsorbed monolayer strongly decreases by increasing the applied load, which translates in a remarkable and unprecedented increase in the tunnel current. These observations are successfully explained using simulations based on the finite element analysis (FEA) and first-principles calculations that permit one to consider the coupling between the mechanical response of the system and the electric dipole variations at the interface.

## 1. Introduction

Central to the success of virtually all applications of nanoparticles (NPs)[1,2] is the need to tailor their properties with organic coatings, often self-assembled monolayers (SAMs), which impact both their stability and specific functionality.[3] Substantial effort has focused on optimizing the activity of the immobilized layer of, for example, antibodies or enzymes. Nevertheless, only recently has the influence of the SAM on the properties of the underlying NP been studied. It has been found that the covering layer might have a remarkable impact on the NP structure. In the case of thiolated molecules, instead of a sharp gold-molecule boundary, a 0.25 nm thick interfacial shell was found to contain enlarged Au–Au distances and an interpenetration of the thiol ligand species.[4,5] Another study revealed that the use of a simple propane thiol monolayer on a nanocrystal was enough to modify its facets.[6]

A large number of questions still remain regarding both the electric and mechanical properties of gold NPs, with and without organic coatings, at the single-NP level. For example, it is still unclear whether the mechanical properties of the NPs are comparable to those of the bulk[6,7] and how they are modified by the presence of organic coatings. Furthermore, although the tuning of the electronic properties of Au NPs by functionalization has been demonstrated,[8,9] the impact of the strain of the covering layer in those changes remains largely unexplored at a quantitative level. Here we present an example of such a quantitative analysis. Our measurements are based on a recently developed technique to grow NPs with an organic coating on only one side and an ohmic contact on the other,[10] a powerful test-bed for molecular electronics.[11] This allows us to address the mechanical and electronic properties of thiolated nanocrystals, using an array of 10 nm facetted nanocrystals with an ohmic bottom contact and a top contact made by an atomic force microscope (AFM) tip at an adjustable loading force. In contrast to the case of extended SAMs on flat surfaces, the use of nano-SAMs (lateral dimensions on the nanoscale) makes the contact area independent of the applied force. Therefore, with this set-up it is possible to measure the load dependence of the mechanical and electronic properties with high precision.

With the fabrication technique reported in ref. 10 (see Methods), half of the nanocrystal is buried in highly doped silicon (Fig. 1a). Its structure is very close to that of an ideal

[a]Institute of Electronics, Microelectronics and Nanotechnology, CNRS, Avenue Poincaré, 59652 Villeneuve d'Ascq, France. E-mail: nicolas.clement@iemn.univ-lille1.fr
[b]Centro de Fisica de Materiales, Centro Mixto CSIC-UPV, Paseo Manuel de Lardizabal 5, Donostia-San Sebastian, Spain
[c]Donostia International Physics Center (DIPC), Paseo Manuel de Lardizabal 4, Donostia-San Sebastián, Spain
[d]IKERBASQUE, Basque Foundation for Science, Bilbao, Spain
[e]Depto. de Física de Materiales UPV/EHU, Facultad de Química, Apdo. 1072, Donostia-San Sebastián, Spain
[f]Laboratory of Chemistry for Novel Materials, Center of Innovation and Research in Materials and Polymers (CIRMAP), University of Mons, UMONS, Place du Parc 20, 7000 Mons, Belgium

†Electronic supplementary information (ESI) available. See DOI: 10.1039/c4nr06180b

‡These authors have equally contributed to the work.

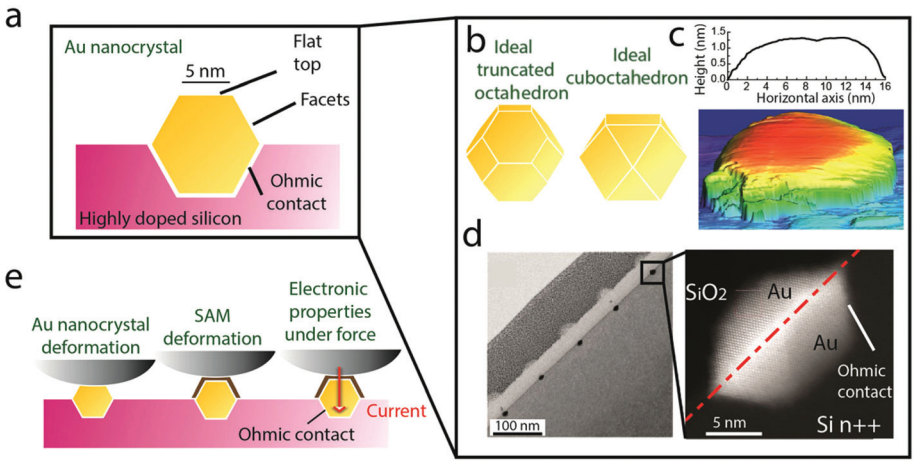


**Fig. 1** Gold nanocrystals: description and experimental setup. (a) Schematic cut-view of the facetted gold nanocrystal. Thanks to the unique fabrication technique (see Methods), these nanocrystals are well attached to a highly doped substrate with an ohmic contact. (b) Fabricated gold nanocrystals resemble either ideally truncated octahedron or cuboctahedron NPs. Annealing temperature (260 °C) was very close to the predicted temperature to obtain these ideal NPs.[12] (c) Scanning Tunneling Microscopy (STM) image obtained on a single Au nanocrystal. The cut line shows a flat top (roughness <2 Å). The green step observed in the STM image is linked to the HF etching prior to imaging in Ultra-High Vacuum (UHV) (partial consumption of highly doped silicon). (d) STEM images taken from ref. 10 on five (left) and single (right) Au nanocrystals. Atoms and facets of the nanocrystal are clearly seen. (e) Schematic view of the experimental setups. From left to right: peak-force AFM on an uncoated nanocrystal, on an alkylthiol-coated nanocrystal and CAFM on a coated nanocrystal.

cuboctahedron or truncated octahedron NP (Fig. 1b).[12] A scanning tunneling microscope (STM) image shows a flat top surface (Fig. 1c) and scanning transmission electron microscopy (STEM) clearly reveals the facets (Fig. 1d) for this NP.[10] This structure is ideal for testing the mechanical properties of naked gold nanocrystals or molecularly functionalized nanocrystals with an AFM tip, for several reasons. First, the force applied with the tip can be precisely tuned. Second, the tip curvature radius (~40 nm) is much larger than the flat top surface of the nanocrystal (<10 nm); thus, this system can be considered as an ideal parallel-plate scenario. Third, statistical analysis can easily be performed using an array with a large number (typically several thousands) of nanocrystals. Finally, due to the ohmic contact between the nanocrystal and the highly doped silicon, the electronic and mechanical properties of the SAM coating can be measured simultaneously with a conducting AFM (CAFM) tip (Fig. 1e).

In this work, we show that the Young's modulus of tiny single crystal NPs (<8 nm in diameter) buried in a silicon substrate is ~20 GPa, smaller than the one of free-standing NPs (~40 nm). We also estimate that the Young's modulus of the alkylthiol monolayers, self-assembled on top of them, is in the range 0.5–2.8 GPa. Electron transport measurements of tiny molecular junctions made with NPs by self-assembled alkylthiol monolayers (chain length from 8 to 18 carbon atoms) reveal unprecedented behaviors: (i) a strong decrease in the tunnel current decay factor $\beta$ from 0.9 to 0.2 per carbon atom when the loading force is increased only up to 30 nN, (ii) a decrease of ~0.4 eV in the HOMO level with respect to the Au Fermi energy. These results are well explained by a force-induced modification of the Au–alkylthiol interface dipole, and supported by DFT calculations.

## 2. Elastic properties

### 2.1. Young's modulus of a gold NP

**Peak-force AFM experimental study.** The mechanical properties are obtained by direct measurement of the deformation with a peak-force Atomic Force Microscope (AFM, Brüker©, see Methods) on an array of nanocrystals at a given load (peak force) of 150 nN (Fig. 2a). This force generates sufficient deformation of the nanocrystal for quantitative study, but is still in the elastic deformation regime. The inset in Fig. 2b shows a zoom on three nanocrystals. Each nanocrystal exhibits a bright ring that indicates a large deformation when the AFM tip is on the facets. When the maximum deformation is measured on the facets and at the center of the top surface for each nanocrystal in a large array of 686 nanocrystals, the constructed deformation histogram reveals two peaks (Fig. 2b) corresponding to the top and the facets. The deformation value on the facets (~3 nm on average) seems large, given the dimensions of the nanocrystal (height of about 2–3 nm; see Fig. 1d). However, one should take into account that peak force deformation measurements are only relevant along the vertical axis and, therefore, the deformations of tilted facets cannot be obtained reliably (see ESI, Fig. S1†). When the tip is on top of the nanocrystal, a total deformation (tip and nanodot) of 0.93 ± 0.08 nm is found experimentally (Fig. 2b). Below, we use FEA to estimate NPs' Young's modulus.

**Finite element analysis of gold nanocrystals' elastic properties.** The experimentally measured deformation is correctly simulated (Fig. 2c) by FEA if we assume a Young's modulus $E_{NP}$ of 20 ± 2 GPa. We considered the full structure including the silicon substrate in which the gold NP is half buried and found a negligible deformation of the substrate (see Fig. S1†).

 

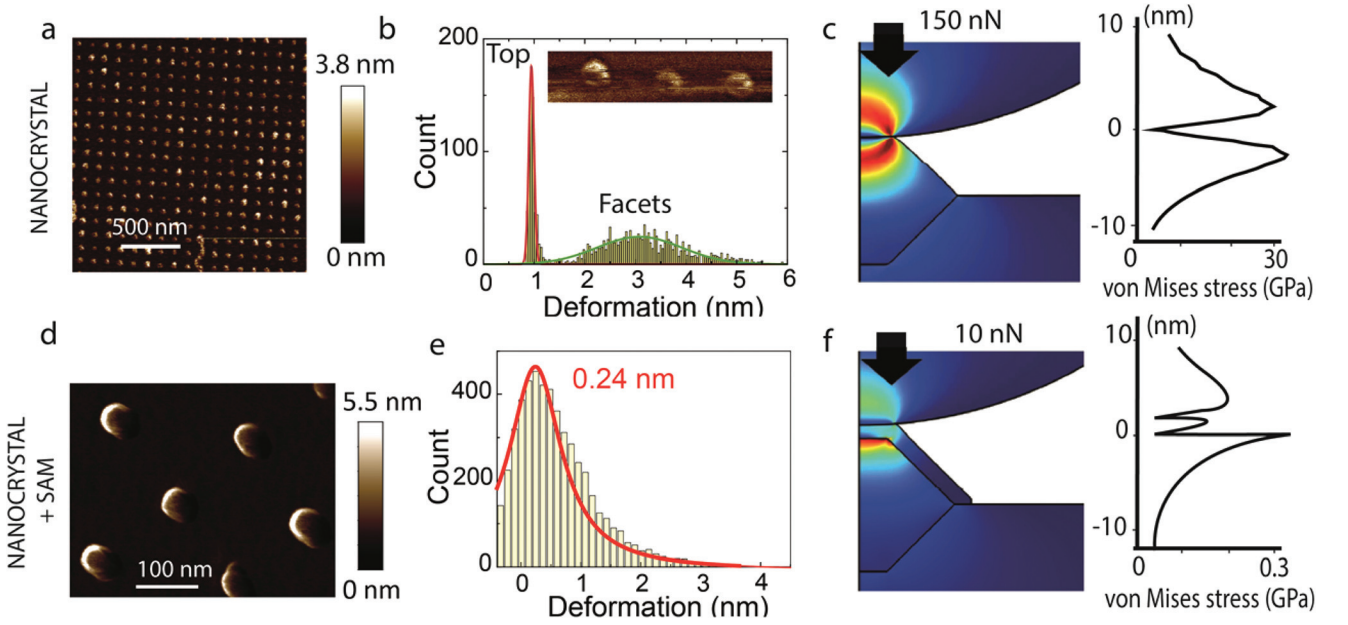


**Fig. 2** Elastic properties of uncoated and coated Au nanocrystals. (a) Peak-force AFM image of the measured deformation on an array of uncoated Au nanocrystals. (b) Histograms of deformation related to the top and the facets of Au nanocrystals. Inset: zoom on three Au nanocrystals. (c) 2D-FEA von Mises stress map of the tip indentation at 150 nN in the Au nanocrystal. NP Young's modulus $E_{NP} \sim 20$ GPa has been selected to get a total deformation of 0.93 nm. This structure, considered as "ideal" might differ from the experimental structure such as the presence of air gap at the gold/Si interface, however the STEM image in Fig. 1c presents a close-to-ideal structure at the atomic resolution. Right: cut view of the von Mises stress along the symmetry axis. (d) Peak-force AFM deformation image of a $C_{12}$-alkylthiolated Au nanocrystal. (e) Histograms of deformation related to the top of coated nanocrystals. (f) 2D-FEA von Mises stress map of the tip indentation in the SAM at 10 nN. SAM's Young's modulus $E_{SAM} \sim 1.4$ GPa has been tuned to get a total deformation of 0.24 nm ($E_{NP} = 20$ GPa).

For FEA, we have chosen to show the von Mises stress, often used in determining whether an isotropic and ductile metal will yield when subjected to a complex loading condition. It has the advantage to clearly delimit each material on the images which is useful for SAM deformation estimation and to highlight the stressed regions. The von Mises stress is equally distributed on both sides of the contact, with the maximum located 4 nm from the contact. The obtained Young's modulus value is lower than the bulk value that is usually considered for $E_{NP}$ (74–80 GPa).[6,7] Below, we discuss the low elastic modulus estimated for sub-10 nm gold nanocrystals.

**Discussion on the 20 GPa gold nanocrystal elastic modulus.** Theoretical studies suggest that the Young's modulus for spherical NPs can be reduced by up to 50% from the bulk value.[13] Previous reports on the elastic properties of gold nanocrystals obtained by time-resolved spectroscopy (mainly nanorods of 20 nm diameter and 100 nm length) have reported either a bulk value[14] (~79 GPa) or lower[15] (~64 GPa). Very recently, it was shown that the Young's modulus is reduced (to ~40 GPa) when the cylindrical symmetry of these nanorods is ruptured by the presence of facets and that this effect is amplified as the length of the nanorod is reduced.[16] This effect was explained by the anisotropic elastic properties of single-crystal nanorods and the heating effect of optically-induced plasmon resonance. Our facetted gold NPs are also single-crystal NPs. As a consequence, the elastic modulus is likely anisotropic with values down to 42 GPa. But even more importantly, we observed microtwins with {111} twin boundaries.[10] Twins likely reduce the elastic modulus of our single-crystal NPs.[17,18] It remains that the large surface to volume ratio may further lower the measured NP elastic modulus.

### 2.2. Young's modulus of SAMs covering gold NPs

**Peak-force AFM experimental study.** Fig. 2d shows the measured deformation, and Fig. 2e the related histograms when a dodecanethiol monolayer (the archetype of a tunnel barrier in molecular junctions[19–24] with 12 carbon atoms) is chemically grafted on the nanocrystals (see Methods). A mean deformation of 0.24 nm is obtained under a pressure of 10 nN (the load is reduced to keep the SAM deformation within the elastic limit). The dispersion (1 nm at half peak) is large but in the range of previously reported deformation dispersion for the laterally extended SAMs (0.3 nm at half peak for the same monolayer and same deformation).[26] There may be a difficulty in making precise deformation measurements in the Å range of such thin layers coating the nanocrystals at the origin of the larger measured dispersion. Below we consider the full width half maximum deformation to estimate the Young's modulus of SAM coated gold NPs, by FEA.

**Finite element analysis and discussion on SAM coated gold nanocrystals.** Based on FEA with $E_{SAM}$, the SAM Young's modulus, we obtain $0.5 < E_{SAM} < 2.8$ GPa. $E_{NP} = 20$ GPa is considered as reported above to take into account the deformation of the NP below the SAM (considering $E_{NP} = 78$ GPa, as pre-

viously reported, would only affect $E_{SAM}$ by 2%). Peak-force AFM images indicate that the adhesion is almost cancelled on alkylthiolated nanocrystals, in agreement with the expected contrast of hydrophilicity/hydrophobicity of $SiO_2$/alkyl SAM (ESI, Fig. S3†). This structure prevents the parasitic role of hydration on the electronic properties of alkylthiolated gold nanocrystals.[25] A similar result is obtained for octanethiol molecules. The FEA simulation reveals a large stress at the monolayer boundary of the NPs (Fig. 2f), the importance of which will be further discussed below. The Young's modulus extracted here for a SAM with 12 methyl groups on a gold nanocrystal is lower than the $E_{SAM}$ of ~4 GPa estimated for closely-packed alkylthiol-functionalized NP arrays[6] (with the assumption of an $E_{NP}$ similar to that of the bulk), but is on a par with the results of Del Rio *et al.*[26] for SAMs on a planar substrate and of Callister *et al.* for polyethylene.[27] Supposing the same "average" Young's modulus $E_{SAM}$ of 1.4 GPa for different alkyl chain lengths $C_N$, where $N$ is the number of carbon atoms, the SAM deformation $\Delta d$ as a function of the loading force obtained by FEA is plotted in Fig. 3a. The observed dependence follows closely that of the Hooke's parallel-plate formula:

$$\Delta d(N) \approx \frac{d_0(N)F}{SE_{SAM}} \quad (1)$$

where $F$ is the applied force, $S$ is the contact area (~55 $nm^2$), and $d_0(8)$ = 1 nm, $d_0(12)$ = 1.5 nm, $d_0(18)$ = 2.5 nm are the theoretical lengths of alkyl chains in their all-*trans* configuration at zero force, which also agree with the average experimental thicknesses measured by AFM (see ESI, Fig. S4†).

Below, we use first-principles density functional theory (DFT) simulations to complement our FEA approach and obtain a molecular-level understanding of the behavior of the monolayer ($C_8$ and $C_{12}$) under an external force.

**First-principles density functional theory.** We studied the effect of the applied force, depending on the length and orientation of the molecules in the SAM, excluding the effects of the substrate and the anchoring groups. The orientation of molecules in the monolayer is defined by three angles (Fig. 3b): tilt ($\theta$), rotational ($\Phi$) and twist ($\psi$). A $\sqrt{3} \times \sqrt{3}$ 30° lattice geometry is assumed for the molecular organization in the SAM on the <111> oriented Au top surface of the nanodots,[9] with an experimental intermolecular distance $d$ of 5.05 Å. Electronic structure calculations and relaxations are described in Methods and ESI (Fig. S5 and S6†).

Fig. 3c shows the variation of the tilt angle under strain for several configurations corresponding to the different values of $\Phi$ and $\psi$. As explained in detail in the ESI† we tilt the molecules as rigid rods using different configurations. This allows obtaining a smooth behavior of the energy *versus* tilt angle

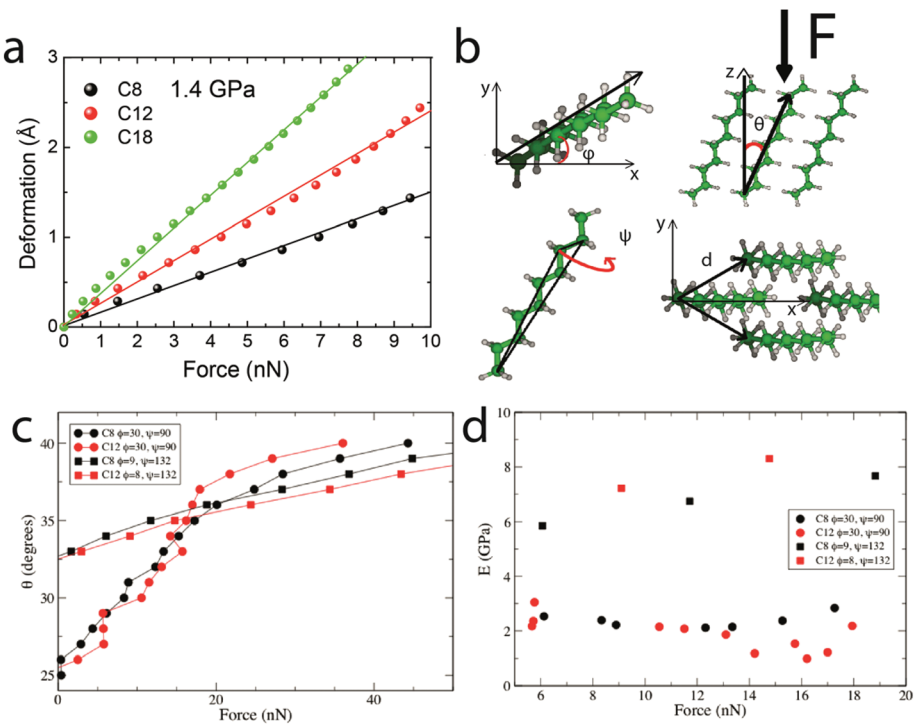


**Fig. 3** Theoretical study of alkyl SAM elastic properties. (a) FEA corresponding to Fig. 2f for 3 different alkyl chain lengths ($C_8$, $C_{12}$, $C_{18}$) at $E_{SAM}$ = 1.4 GPa. A linear deformation is not observed with a planar SAM (*i.e.*, a SAM with a large lateral extension grafted on an Au surface), in which, due to the tip indentation into the SAM, the contact area increases with force (ESI, Fig. S2†). (b) Schematic view of the SAM representation. The molecular tilt angle $\theta$ is the angle between the molecular principal axis and the surface normal while $\Phi$ and $\Psi$ represent the rotational and twist angles, respectively. The parameter $d$ is the intermolecular distance. (c) Tilt *versus* force for two possible configurations of the $C_8$ and $C_{12}$ SAM estimated from DFT calculations. (d) Estimated Young's modulus $E$ for $C_8$ and $C_{12}$ as a function of the applied force from DFT calculations.

 

that can be numerically differentiated. Although the deformation properties barely depend on the chain length (*i.e.*, the tilt angle-force dependence is the same for the $C_8$ and $C_{12}$ molecules), they strongly depend on ($\Phi$, $\psi$) as shown in the ESI.† This highlights the dependence of the calculated elastic constants on the detailed structure of the layer, which agrees with the large variance in the measured Young's modulus. An initial analysis of the energy landscape for a tilt angle $\theta = 30°$, close to the equilibrium value at zero load, reveals the minimum of energy around (8°, 132°) for both the molecules. Using this configuration we obtain an estimation of the Young's modulus for the applied load in the range 0–20 nN of $E_{SAM} \sim 7$ GPa [our definition of the Young's modulus for finite deformation can be found in eqn (S1) of the ESI†].[28–30] This value is considerably larger than our experimental estimation. However, we must take into account that our estimations provide the upper limits for the Young's modulus of the layer. Indeed, it is easy to find starting configurations that are not far in energy and give rise to "softer" layers. Under applied stress these "softer" configurations will be the most relevant, since configurations with a large Young's modulus will be rapidly destabilized as a function of the applied stress (since their energy increases faster). For example, for the (30°, 90°) configuration we estimate an $E_{SAM} \sim 2$ GPa for both the $C_8$ and $C_{12}$ molecules, which is fairly independent of the applied force as shown in Fig. 3d. This result is close to the experimental and FEA values. The fact that the values of $E_{SAM}$ estimated by first-principles DFT calculations using plausible monolayer configurations are close to those obtained from the experiments can be interpreted as a validation of the FEA approach. In the Electronic properties section below, we consider the SAMs as homogeneous films with a constant Young's modulus.

### 2.3. Electronic properties

**Current histograms generated by CAFM on a large array of thiolated gold NPs.** At a given load and bias, the electronic properties of the SAM can be investigated by Conducting AFM (CAFM, Fig. 4a, inset and Methods). The bridging of metal electrodes by alkanes (simple saturated carbon chains) is used as a prototype tunnel junction for investigating the electronic and transport properties across molecule–electrode interfaces.[20–23,29,30] Alkanes have a large energy gap (of several eV) between the highest occupied and the lowest unoccupied molecular orbital (HOMO–LUMO gap).[21,31–33] Alkane junctions display typical off-resonance transport characteristics as the Fermi energy $E_F$ of the metal electrodes falls into the insulating HOMO–LUMO gap. The low-bias tunnelling probability of electrons can be understood in terms of an energy barrier $\varphi$, related to the position and alignment of the molecular level with respect to $E_F$, and a tunneling length set by the number of carbon atoms in the molecular backbone. Because alkylthiolated nanocrystals have a lower resistivity than native silicon

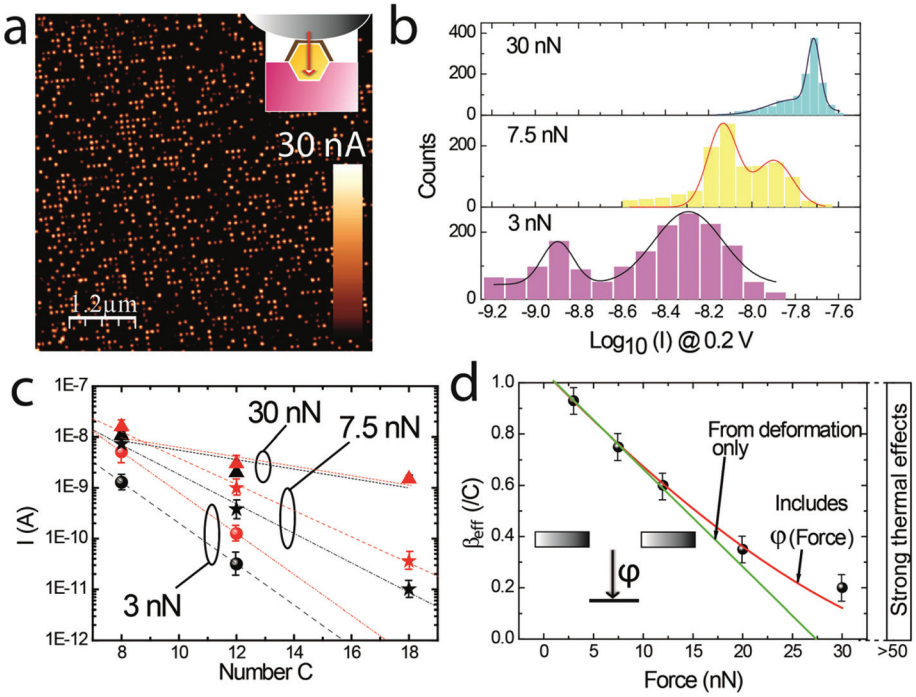


**Fig. 4** Electronic properties of alkylthiolated gold nanocrystals. (a) CAFM image of $C_8$-coated Au nanocrystals at 0.2 V and 30 nN. Inset: schematic view of the experimental setup. (b) Current histograms for $C_8$-coated nanocrystals at 0.2 V and 3 different loads. The number of counts is about 1600 per histogram. (c) Current *vs.* number of carbon atoms for $C_8$, $C_{12}$, $C_{18}$ at 3 different loads. Each point corresponds to the maximum of a peak in the current histograms. Two colors (black and red) are used to distinguish between both peaks. (d) $\beta_{eff}$ obtained from (c), is plotted as a function of force. Inset: band diagram showing the potential $\varphi$ between the HOMO and the Fermi levels of the electrodes. The $\beta_{eff}$ decreases rapidly with the force increasing from 0 to 30 nN (Fig. 4d) and above 50 nN, Joule-induced heating is observed on $C_8$ SAMs, leading to nanocrystal sublimation (ESI, Fig. S6†).

oxide, they are clearly distinguished in the CAFM image (Fig. 4a).[11] Due to the linear scale, bright spots mainly correspond to high conductance junctions. After thiol adsorption and cleaning in an ultrasonic bath, typically 80–85% of the dots are still there (see ESI, Fig. S3 and S11†). The 15–20% remaining dots are sometimes lying on the surface but do not respond electrically because of the presence of a native oxide layer. As a consequence, they are not considered in the statistical study.

Histograms of the current are generated from the CAFM image, with one count per nanocrystal. Histograms for $C_8$ at 3, 7.5 and 30 nN are shown in Fig. 4b. Two peaks of conductance, fitted by two log-normal distributions (see ESI, Fig. S7†), can be observed. They are attributed to different molecular organization phases in the SAM,[11,34] and tend to merge when the applied force is increased. The distribution is rather large but in the same range as the one typically observed in single-molecule break junction experiments.[35] The mean current level increases up to several orders of magnitude with a load of 3 to 30 nN (Fig. 4b and 4c).

**Discussion on the tunnel decay rate.** If we assume a model where the SAM acts as a tunneling barrier, then the conductance can be defined as $G = Ae^{-\beta_{eff}N}$ where $A$ is the contact conductance and $N$ the number of carbon atoms. The decay constant $\beta_{eff}$, extracted by fitting the current $I$ *vs.* $N$ log-lin plots shown in Fig. 4c supposing $A$ constant,[35–38] is a parameter including both the variation of the tunnel barrier height and the tunnel distance (*i.e.*, SAM thickness) with the applied force. $\beta_{eff}$ is not strictly equal for the two conductance peaks, but for simplicity, we considered a single $\beta_{eff}$ for both peaks with an error bar (Fig. 4d). $\beta_{eff}$ decreases rapidly on increasing the force from 0 to 30 nN and above 50 nN, Joule-induced heating is observed on $C_8$ SAMs, leading to nanocrystal sublimation (see ESI, Fig. S8†). As $\beta_{eff}$ tends to zero, the measured current level barely depends on the number of carbon atoms in the monolayer. For comparison, in planar alkyl SAMs, $\beta_{eff}$ remains above 0.75.[41] The most representative effect is the current level for $C_{18}$, which is negligible at 3 nN and becomes similar to that of $C_8$ at 30 nN. This finding is partly related to the fact that $C_{18}$ SAMs are more deformed under strain than $C_8$ SAMs (Fig. 3a).

Considering the SAM deformations $\Delta d$ determined above (eqn (1) and Fig. 3a), the force-dependent $\beta_{eff}$ is written as

$$\beta_{eff} = \beta_0\sqrt{\frac{\varphi}{\varphi_0}}\left[1-\frac{\Delta d}{d_0}\right] \approx \beta_0\sqrt{\frac{\varphi}{\varphi_0}}\left[1-\frac{F}{SE_{SAM}}\right] \qquad (2)$$

where $\beta_0$ and $\varphi_0$ are the tunnel decay ratio and the tunnel barrier height, respectively, when no force is applied on the SAM; and $\varphi(F)$ is the average force-dependent tunnel barrier (Fig. 4d). In the first step (considering only the monolayer deformation, *i.e.* $\varphi = \varphi_0$), a good fit is obtained (Fig. 4d) for $F < 10$ nN with $\beta_0 = 1.05$ per carbon atom, and using $E_{SAM} = 0.7$ GPa (in the range of measured values). $\beta_0$ is in agreement with the values previously reported for the alkyl chains (0.8–1.2 per carbon atom)[20–22,35,36] either for SAMs or single-molecule junctions and either for monothiol or dithiol junctions, as discussed more extensively in review papers.[39,40] Above 10 nN, we observe (Fig. 4d) a deviation of $\beta_{eff}$ from linear dependence, which can be ascribed to an additional effect such as a possible dependence of the tunnel energy barrier on force. To check this issue, the transition voltage spectroscopy (TVS) method is used to determine the energy position of the molecular orbital in the junction.[42–46]

**TVS technique to discuss the force-induced HOMO level shift.** In this method, the energy barrier height, namely the energy offset $\varphi$ (Fig. 4d) between the Fermi energy of the metal electrode and one of the molecular orbitals, is estimated from the current–voltage ($I$–$V$) measurement (see Methods). In the interpretation of electron transport through a tunnelling barrier, the voltage at which a minimum is observed in this plot represents the transition voltage $V_T$ between the direct and the Fowler–Nordheim tunnelling regime. In the case of molecular junctions, $V_T$ can estimate the energy position of the molecular orbital (relative to the Fermi energy of the electrodes) involved in the transport mechanism (here, we suppose that for the Au/alkylthiol junctions the HOMO level[35,36] dominates transport, see the discussion below), *via* a simple relationship $\varphi = \alpha V_T$, with $\alpha \sim 0.87$ for symmetric barriers.[47]

We performed direct spectroscopic $I$–$V$ measurements on an alkylthiolated nanocrystal with $C_8$ molecules (C-AFM tip at a stationary point contact on the nanodot junctions, see Methods) representative of each conductance peak (*i.e.*, measured on nanodot molecular junctions belonging to the maximum of each peak). Replotting the $I$–$V$ curves (Fig. 5a) as TVS plots (Fig. 5b), we obtain the $V_{TLC}$ and $V_{THC}$ for the low-conductance and high-conductance peaks, respectively. The Pt top and Au bottom electrodes work functions are in the same range and do not induce significant asymmetry (see ESI, Fig. S9†). The results of $\varphi \sim 0.87\ V_T$ are shown in Fig. 5c for $C_8$, $C_{12}$ and $C_{18}$ molecules at forces up to 30 nN. For all nanodot junctions, the $\varphi$ values at a low force are in the range of the previously reported values for alkylthiol junctions on Au (1–1.9 V).[35–42] We observe a linear dependence of $\varphi$ on the applied force

$$\varphi = \varphi_0 - aF \qquad (3)$$

with $\varphi_0 = 1.25 \pm 0.15$ eV and $a \sim 0.013$–$0.03$ eV nN$^{-1}$ (Fig. 5c). When we use eqn (3) with averaged "$a$" in eqn (2), we obtain a good fit of the whole $\beta_{eff}$ *vs.* force curve (Fig. 4d, other parameters in eqn (2) unchanged).

**Discussion on electronic properties and interfacial dipoles.** Such a large force modulation of $\beta_{eff}$ and the position of the HOMO level in molecular junctions were not previously observed on C-AFM measurements for SAMs with a large lateral extension on the Au substrate electrode. These previous results are puzzling and contradictory, showing that $\beta_{eff}$ is almost constant[48,49] or slightly increasing[50] or decreasing[51] with the C-AFM loading force. This difference can be due to several reasons: (i) in contrast to our case, the contact area is increased with force and consequently the force per surface

 

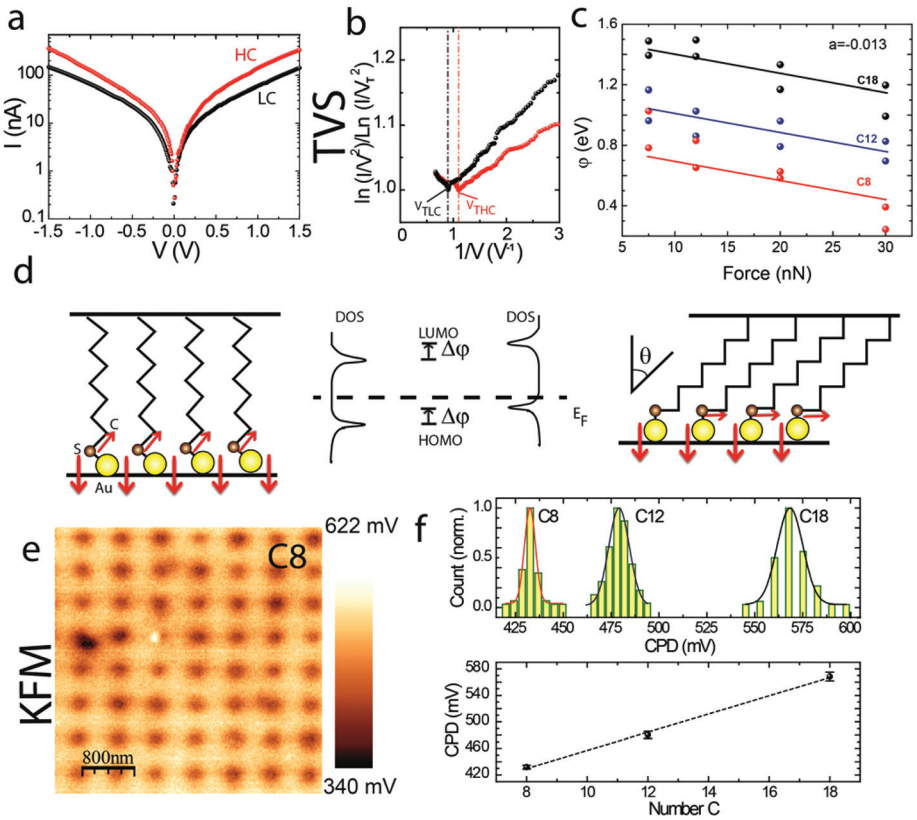


**Fig. 5** Molecular orbital positions of alkylthiolated gold nanocrystals. (a) *I*–*V* for the two representative curves of the high and low conductance peaks for $C_8$ molecules. (b) Normalized TVS obtained from (a) used to extract minima $V_{TLC}$ and $V_{THC}$ relative to low-conductance and high-conductance peaks, respectively. (c) $\varphi = 0.87\ V_T$ is plotted as a function of force for $C_8$, $C_{12}$ and $C_{18}$ SAMs. Parameter *a* is extracted from these data using eqn (3). (d) Schematic picture proposed in ref. 48, to denote the tilt-dependent molecular gate effect arising from changes in the effective interfacial dipole (vector sum of the red arrows), which has contributions from a permanent surface dipole and a molecular dipole oriented along the S–C bond. When the molecules are tilted by $\theta$, the perpendicular component (with respect to the surface) of the molecular S–C bond dipole gets reduced and the work function of the decorated surface increases. As sketched, this results in an upward shift of the molecular orbitals with respect to the Fermi energy, and hence in an enhanced tunnelling through the tail of HOMO resonance. (e) KFM CPD image for $C_8$ decorated Au nanocrystals. (f) CPD histograms (up) for $C_8$, $C_{12}$ and $C_{18}$ decorated Au nanocrystals. The increased tilt angle for short molecules tends to reduce the molecular dipole. When CPD is plotted as a function of the number of C, a linear dependence is obtained (slope 14 mV $C^{-1}$). We obtained CPD = 220 mV for the reference sample with uncoated Au nanocrystals (see ESI†).

unit is not constant; (ii) these previous experiments used SAMs on polycrystalline evaporated Au, thus the Au/alkylthiol interface may have hindered the behaviour reported in our work.

Studies based on DFT calculations also show that $E_{HOMO}$ (the energy of the HOMO level referred to the Fermi level of the substrate) increases and $\varphi$ decreases with an increased tilt angle $\theta$ (Table 1) due to the interfacial dipole (Fig. 5d) that is expected to be located between the sulfur and the first carbon atom.[52,53] Moreover, $\varphi(F)$, derived from $\varphi(\theta)$ (see Table 1), shows a linear decrease with the applied force and *a*, extracted from eqn (3), is in agreement with the experimental results. As a simple picture, the tilt angle increases with load while the interfacial dipole is reduced. The large stress arising at the NP interface below the SAM (320 MPa @ 10 nN, Fig. 2f) could also play a role in $\varphi(F)$ through a modification of the NP's work function.[54,55] However, considering a typical bandgap pressure coefficient for NPs (<10 mV/100 MPa),[54,55] the estimated $\Delta\varphi$, due to the sole Au NP work function, would have been lower than 15% of the measured effect.

The $\varphi$–*F* results obtained for alkylthiolated NPs from $\beta_{eff}$–*F*, using the TVS technique, and DFT calculations converge to a value of $a \sim 0.025$ eV $nN^{-1}$ (eqn (3)). This result is one order of magnitude larger than the value reported for molecular junctions on a planar substrate.[41] In addition, the proposed mechanism of tilt-dependent interfacial S–C dipole projection perpendicular to the NP interface, also differs from the previous suggestion[41] of the thickness-dependent field effect, such as image-charge.

**Interfacial dipoles investigated by Kelvin probe force microscopy.** We further examined the role of interfacial dipoles in thiolated NPs by considering the reduction of $\varphi$ with the alkyl chain length at low force (Fig. 5c). Smaller alkylthiol SAMs have a larger tilt angle because the van der Waals forces between the molecules are reduced.[56] This observation is compatible with the interfacial dipole hypothesis.

**Table 1** Comparison of the force coefficient *a* obtained from DFT and experiments. Variation of $E_{HOMO}$ (the energy of the HOMO referred to the Fermi energy of the substrate) *versus* the tilt angle taken from ref. 48 and 49 for $C_8$ and $C_{12}$ dithiol molecules. Here we use the relationship $F = (1 - \cos\theta)\cdot E_{SAM}\cdot S$ with $E_{SAM}$ = 0.7 GPa, corresponding to the value obtained from the $\beta$–$F$ curves (Fig. 3d). $\Delta\varphi$ gives the movement of $E_{HOMO}$ with respect to the reference at $\theta$ = 0. From the calculated slope of $\Delta\varphi(F)$ we obtain a theoretical estimation of the parameter *a* in eqn (3), [we also show that the corresponding values of $E_{SAM}$ are allowed to change within the experimental estimates 0.5–2.8 GPa] in the range of the experimental results obtained by TVS (Fig. 5c)

| Molecule | $\theta$ (deg) | $F$ (nN) = $(1 - \cos\theta)$ $E_{SAM}\cdot S$ | $E_{HOMO}$ | $\Delta\varphi$ (eV) | Theoretical (eV nN$^{-1}$) from DFT | Experimental (eV nN$^{-1}$) from TVS |
|---|---|---|---|---|---|---|
| $C_8$ | 0 | 0 | −3.05 | 0 | | |
| | 26 | 4 | −2.81 | −0.24 | 0.077 (0.019–0.108) | 0.03 |
| | 35 | 7 | −2.44 | −0.61 | | |
| $C_{12}$ | 0 | 0 | −2.9 | 0 | | |
| | 30 | 5 | −2.54 | −0.36 | 0.062 (0.016–0.088) | 0.014 |
| | 50 | 14 | −2.08 | −0.82 | | |

Kelvin probe force microscopy (see Methods and ESI, Fig. S10†) image obtained on $C_8$ is shown in Fig. 5e. From similar measurements on $C_{12}$ and $C_{18}$, we built contact potential difference (CPD) histograms (between the SAM and the tip). They reveal that the CPD measured on the alkylthiolated nanocrystals increases linearly (14 mV C$^{-1}$) with the chain length (Fig. 5f). This feature corresponds to a decrease in the work function of the alkylthiolated Au ($W_{Au}$) when increasing the chain length. This result is compatible with the dipolar representation in Fig. 5d. From the Helmholtz equation (see ESI†), we deduce that the perpendicular projection of the Au/SAM dipole ($\mu_z$) decreases from ~0.6 D (for $C_{18}$) to ~0.35 D (for $C_8$). The smaller the chain length, the higher is the tilt angle and the smaller is the S–C $\mu_z$. The CPD results on thiolated NPs are in the same range as those obtained on thiolated gold substrates,[57] and are also at par with Ultraviolet Photoelectron Spectroscopy (UPS) measurements.[58] The force-dependent experiments presented here, together with DFT simulations and the KFM experiment suggest that charge transport occurs through the HOMO level (Fig. 5d). In fact, an increase of $W_{Au}$, when decreasing the chain length, would correspond to an increase in the energy barrier height with the LUMO and a decrease in the energy barrier with the HOMO (Fig. 5d). According to our TVS results (Fig. 5c), we can conclude that there was a HOMO mediated transport in our case.

## 3. Conclusions

Here, we describe the elastic and electronic properties of alkylthiolated gold nanocrystals. We find that the estimated Young's modulus of pure facetted gold NPs is four times smaller than the usually considered bulk modulus, which could be explained by the recent suggestion[16] that anisotropy in elastic properties should be considered for single-crystal NPs, the presence of twins in our NPs and the large surface to volume ratio. We also estimated the Young's modulus of the alkylthiol monolayer to be ~1.4 GPa, by combining the AFM measurements of monolayer deformation and FEA simulations. This value is consistent with the results of structural relaxations based on DFT calculations that estimate the Young's modulus of the layer as a function of the rotational and twist angles. The nanoscale molecular junctions formed by these alkylthiolated nanocrystals contacted by a CAFM tip show strong decreases in the tunnel decay constant $\beta(F)$ and in the effective potential barrier height $\varphi(F)$ as a function of applied force even in the few nN regime. Combined with FEA and *ab initio* calculations, these results are satisfactorily explained by the strain-induced molecular deformation and the strong impact of the interfacial dipole on the molecular orbital position. This study at the single nanocrystal level provides a reference model system for the elastic and electronic properties of NPs, important for various NP-based applications such as strain gauges[59] and self-powered triboelectric sensors.[60] As the SAM Young's modulus is not expected to change significantly with complexity, these results should be partly transposed to different organic coatings with a consideration of lower $\beta_0$ for π-conjugated oligomers. In addition, linkers composed of a thiol bond and a short alkyl chain are often part of more complex molecules, including biomolecules, which suggests a similar contribution from interfacial dipoles. These findings show that even small van der Waals interactions in the nN range,[61] for example between NPs or between NPs and carbon nanotubes[62] or graphene, could be sufficient to alter the electronic properties of a wide variety of NP-based molecular devices. Similar measurements would be of great interest to other "functional" molecular junctions, such as "mechanical" switches (diarylethene, azobenzene) in which the applied force may also impact the isomerization, and thus the electrical conductance switching of these molecular devices.

## 4. Methods

### 4.1. Self-assembled monolayers (SAMs)

For SAM deposition, we exposed the freshly evaporated gold nanodots to a 1 mM solution of alkylthiols (from Aldrich) in ethanol (VLSI grade from Carlo Erba) for 15 h. Then, we rinsed the treated substrates with ethanol followed by cleaning in an

 

ultrasonic bath of chloroform (99% from Carlo Erba) for 1 min.

### 4.2. AFM (peak-force, C-AFM and KFM)

Peak-force AFM measurements were performed with the recently developed peak force tapping mode (Dimension ICON, Brüker, PeakForce-Quantitative Nano-Mechanics). Silicon cantilevers (Bruker AXS©) with a spring constant of 150–250 N $m^{-1}$ were used for experiments on uncoated Au nanocrystals and of 0.1–0.3 N $m^{-1}$ for coated Au nanocrystals. Cantilever spring constant and sensitivity were calibrated before and after each experiment. In the present experiment, we did not use the DMT modulus package to directly obtain an image of the Young's modulus; this model is not appropriate for nanocrystals that have a dimension much smaller than the tip curvature radius. As a consequence, we have selected the direct measurement of deformation that can be converted into a Young's modulus by FEA. Data processing was performed using the commercial Nanoscope Analysis software (Bruker AXS©) and Wsxm (Nanotec.es).[63]

We performed current voltage measurements by conducting atomic force microscopy (C-AFM) under an $N_2$ atmosphere (Dimension 3100, Veeco), using a PtIr coated tip (same tip for all C-AFM measurements). The tip curvature radius is about 40 nm (estimated by SEM), and the force constant is in the range 0.17–0.2 N $m^{-1}$. The conductance of the Au nanodot without a molecule is much larger than that for Au nanodots with molecules and, in that case, dots are often burnt after/during such measurements probably due to the large current density. In the scanning mode, the bias is fixed and the tip sweep frequency is set at 0.5 Hz. Since our experimental setup is limited to 512 pixels per image, it leads to a typical number of counts of 2700 for a 6 × 6 μm C-AFM image. In the spectroscopy mode, representative molecular junctions belonging to each conductance peak are first identified from the C-AFM image. Because of the imprecise positioning of the tip, 100 spectroscopic *I–V* curves are taken around this dot using a square grid (10 × 10 points with a lateral step of 2 nm). A significant current can only be measured when the tip is on top of the dot and thus a single *I–V* (with the maximum current) from these 100 *I–V* curves is selected per dot. TVS is obtained by plotting the *I–V* data in the form of a Fowler–Nordheim plot ($\ln(I/V^2)$).

The KFM measurements were conducted using a Dimension 3100 atomic force microscopy (AFM) system in a controlled nitrogen environment glove box. We used Pt/Ir (0.95/0.05) metal-plated cantilevers with a spring constant of ~3 N $m^{-1}$ and a resonance frequency of ~70 kHz. First, the height profile was recorded in tapping mode. Then the potential or phase profiles were measured in the noncontact lift mode at a height of 25 nm above the surface.

### 4.3. Nanodot histograms

We used the OriginC program developed by us for the threshold analysis (given in the ESI†). One count corresponds to the maximum current for one nanodot.

### 4.4. FEA

COMSOL v4.3 with structure and deformation package was used to evaluate the Young's modulus of both the NP and SAMs. The design was performed in 2D-axisymmetry to simplify calculations. The tip and silicon substrate Young's moduli of 170 GPa and 131 GPa, respectively, were considered.

### 4.5. DFT calculations

The monolayer was modeled using periodic boundary conditions with one molecule in each unit cell. The orientation of the molecule in the monolayer is defined by the three angles shown in Fig. 3b. A $\sqrt{3} \times \sqrt{3}$ 30° lattice was assumed with the experimental intermolecular distance $d$ = 5.05 Å. Several structural relaxations were performed as explained in the ESI.† First the tilt angle $\theta$ of the molecules was fixed to the commonly reported value of 30° and the relevant values of ($\Phi$, $\psi$) were determined by exploring the energy landscape. Afterwards the energy *versus* tilt curve was obtained for several configurations with fixed values ($\Phi$, $\psi$). We chose this approach to determine, on the one hand, the dependence of the results on the details of the structure and, on the other hand, to obtain smooth curves that would allow numerical differentiation to obtain an estimation of the $F(\theta)$ curves. The electronic structure calculations and the relaxations were performed with the DFT code SIESTA[64] using a real-space grid of 400 Ry and a double-ζ plus polarization (DZP) basis for the C, and H atoms with an energy shift of 0.02 Ry. We used a Brillouin zone sampling of 6 × 6 × 1 *k*-points. The height of the supercell in the *z*-direction was fixed as 25 Å for $C_8$ and 30 Å for $C_{12}$, so there was enough vacuum to avoid interactions among periodic replicas of the monolayers. The total energy was converged with respect to these parameters.

## Acknowledgements

The authors would like to thank R. Arinero from IES Montpellier, T. Melin from IEMN for their fruitful comments, and S. Lamant, J. Oden for assistance in FEA. P.L. is a Senior Research Associate from the Fund for Scientific Research of Belgium (F.R.S. – FNRS). K.S. has been supported by the Nord-Pas-de Calais Council fund and the ANR project SAGE III-V (no. ANR11BS1001203) and S.D. by EU project I-ONE (FP7 no. 280772). The experiments were partly funded by the SINGLEMOL project supported by the Nord-Pas-de Calais council fund. We also acknowledge funding from the Basque Government (Grant No. IT-756-13) and the Spanish MINECO (Grant Nos. MAT2013-46593-C6-2-P and FIS2013-48286-C2-2-P).

## Notes and references

1 M. C. Daniel and D. Astruc, *Chem. Rev.*, 2004, **104**, 293.
2 M. Ferrari, *Nat. Rev. Cancer*, 2005, **5**, 161.
3 J. C. Love, L. A. Estroff, J. K. Kriebel, R. G. Nuzzo and G. M. Whitesides, *Chem. Rev.*, 2005, **105**, 1103.

4 P. D. Jadzinsky, G. Calero, C. J. Ackerson, D. A. Bushnell and R. D. Kornberg, *Science*, 2007, **318**, 430.
5 I. L. Garzon, C. Rovira, K. Michaelian, M. R. Beltran, P. Ordejon, J. Junquera, D. Sanchez-Portal, E. Artacho and J. M. Soler, *Phys. Rev. Lett.*, 2000, **85**, 5250.
6 M. Watari, R. A. MacKendry, M. Vögtli, G. Aeppli, Y.-A. Soh, X. Shi, G. Xiong, X. Huang and I. K. Robinson, *Nat. Mater.*, 2011, **10**, 862.
7 K. E. Mueggenburg, X.-M. Lin, R. H. Goldsmith and H. M. Jaeger, *Nat. Mater.*, 2007, **6**, 656.
8 P. Zhang and T. K. Sham, *Appl. Phys. Lett.*, 2002, **81**, 736.
9 S. J. van der Molen, J. Liao, T. Kudernac, J. S. Agutsson, L. Bernard, M. Calame, B. J. van Wees, B. L. Feringa and C. Schönenberger, *Nano Lett.*, 2009, **9**, 76.
10 N. Clément, G. Patriarche, K. Smaali, F. Vaurette, K. Nishiguchi, D. Troadec, A. Fujiwara and D. Vuillaume, *Small*, 2011, **7**, 2607.
11 K. Smaali, N. Clément, G. Patriarche and D. Vuillaume, *ACS Nano*, 2012, **6**, 4639.
12 A. S. Bernard, N. P. Kirland, A. I. van Huis and H. Xu, *ACS Nano*, 2009, **3**, 1431.
13 R. Dingreville, J. Qu and M. J. Cherkaoui, *J. Mech. Phys. Sol.*, 2005, **53**, 1827.
14 P. Zijlstra, A. L. Tchebotareva, J. W. M. Chon, M. Gu and M. Orrit, *Nano Lett.*, 2008, **8**, 3493.
15 M. Hu, P. Hillyard and G. V. Hartland, *Nano Lett.*, 2004, **4**, 2493.
16 M. A. Mahmoud, D. O'Neil and M. A. El-Sayed, *Nano Lett.*, 2014, **14**, 743.
17 Y. Tang and M. Ouyang, *Nat. Mater.*, 2007, **6**, 754.
18 V. Yamakov, D. Wolf, S. R. Phillpot, A. K. Mukherjee and H. Gleiter, *Nat. Mater.*, 2002, **1**, 45.
19 B. Mann and H. Kuhn, *J. Appl. Phys.*, 1971, **42**, 4398.
20 R. E. Holmlin, R. Haag, M. L. Rustem, F. Ismagilov, A. E. Cohen, A. Terfort, M. A. Rampi and G. M. Whitesides, *J. Am. Chem. Soc.*, 2001, **123**, 5075.
21 W. Wang, T. Lee and M. A. Reed, *Phys. Rev. B: Condens. Matter*, 2003, **68**, 035416.
22 D. J. Wold and C. D. Frisbie, *J. Am. Chem. Soc.*, 2001, **123**, 5549.
23 V. B. Engelkes, J. M. Beebe and C. D. Frisbie, *J. Am. Chem. Soc.*, 2004, **126**, 14287.
24 D. Xiang, H. Jeong, T. Lee and D. Mayer, *Adv. Mater.*, 2013, **25**, 4845.
25 D. P. Long, J. L. Lazorcik, B. A. Mantooth, M. H. Moore, M. A. Ratner, A. Troisi, Y. Yao, J. W. Ciszek, J. M. Tour and R. Shashidhar, *Nat. Mater.*, 2006, **5**, 901.
26 F. W. Del Rio, C. Jaye, D. A. Fischer and R. F. Cook, *Appl. Phys. Lett.*, 2009, **94**, 131909.
27 W. D. Callister, *Materials Science and Engineering: An introduction*, Wiley, New York, 2000.
28 A. Ulman, *An Introduction to Ultrathin Organic Films: From Langmuir-Blodgett to Self-Assembly*, Academic Press, San Diego, CA, 1991.
29 D. Vuillaume, *Proc. IEEE*, 2010, **98**, 2111.
30 H. Haick and D. Cahen, *Prog. Surf. Sci.*, 2008, **83**, 217.
31 C. Boulas, J. V. Davidovitz, F. Rondelez and D. Vuillaume, *Phys. Rev. Lett.*, 1996, **76**, 4797.
32 D. Vuillaume, C. Boulas, J. Collet, G. Allan and C. Delerue, *Phys. Rev. B: Condens. Matter*, 1998, **58**, 16491.
33 J. K. Tomfohr and O. F. Sankey, *Phys. Rev. B: Condens. Matter*, 2002, **65**, 245105.
34 E. Barrena, E. Palcios-Lidon, C. Munuera, X. Torrelles, S. Ferrer, U. Jonas, M. Salmeron and C. Ocal, *J. Am. Chem. Soc.*, 2004, **126**, 385.
35 L. Venkataraman, J. E. Klare, I. W. Tam, C. Nuckolls, M. S. Hybertsen and M. L. Steigerwald, *Nano Lett.*, 2006, **6**, 458.
36 B. Xu and N. J. Tao, *Science*, 2003, **301**, 1221.
37 S. Guo, J. Hihath, I. Diez-Perez and N. Tao, *J. Am. Chem. Soc.*, 2011, **133**, 19189.
38 D. Xiang, H. Jeong, T. Lee and D. Mayer, *Adv. Mater.*, 2013, **25**, 4845.
39 A. Salomon, D. Cahen, S. Lindsay, J. Tomfohr, V. B. Engeles and C. D. Frisbie, *Adv. Mater.*, 2003, **15**, 1881.
40 D. Vuillaume, *C. R. Phys.*, 2008, **9**, 78.
41 G. Wang, T.-W. Kim, G. Jo and T. Lee, *J. Am. Chem. Soc.*, 2008, **131**, 5980.
42 J. M. Beebe, B. Kim, J. W. Gadzuk, C. D. Frisbie and J. G. Kushmerick, *Phys. Rev. Lett.*, 2006, **97**, 026801.
43 J. M. Beebe, B. Kim, J. W. Gadzuk, C. D. Frisbie and J. G. Kushmerick, *ACS Nano*, 2008, **2**, 827.
44 J. Chen, T. Markussen and K. S. Thygesen, *Phys. Rev. B: Condens. Matter*, 2010, **82**, 121412.
45 E. H. Huisman, C. M. Guédon, B. J. van Wees and S. J. van der Molen, *Nano Lett.*, 2009, **9**, 3909.
46 G. Ricoeur, S. Lenfant, D. Guérin and D. Vuillaume, *J. Phys. Chem. C*, 2012, **116**, 20722.
47 I. Baldea, *Phys. Rev. B: Condens. Matter*, 2012, **85**, 035442.
48 V. B. Engelkes and C. D. Frisbie, *J. Phys. Chem. B*, 2006, **110**, 10011.
49 H. Song, H. Lee and T. Lee, *Ultramicroscopy*, 2008, **108**, 1196.
50 V. B. Cui, *et al.*, *Nanotechnology*, 2002, **13**, 5.
51 D. S. Wold and C. D. Frisbie, *J. Am. Chem. Soc.*, 2001, **123**, 5549.
52 T. Frederiksen, C. Munuera, C. Ocal, M. Brandbyge, M. Paulsson, D. Sanchez-Portal and A. Arnau, *ACS Nano*, 2009, **3**, 2073.
53 G. Foti, D. Sanchez-Portal, A. Arnau and T. Frederiksen, *J. Phys. Chem. C*, 2013, **117**, 14272.
54 A. M. Smith, A. M. Mohs and S. Nie, *Nat. Nanotech.*, 2009, **4**, 56.
55 S.-H. Wei and A. Zunger, *Phys. Rev. B: Condens. Matter*, 1999, **60**, 5404.
56 J. C. Love, L. A. Estroff, J. K. Kriebel, R. G. Nuzzo and G. M. Whitesides, *Chem. Rev.*, 2005, **105**, 1103.
57 J. Lü, E. Delamarche, L. Eng, R. Bennewitz, E. Meyer and H.-J. Güntherodt, *Langmuir*, 1999, **15**, 8184.
58 D. M. Alloway, M. Hofmann, D.-L. Smith, N. E. Gruhn, A. L. Graham, R. Colorado, V. H. Wysocki, T. R. Lee, P. A. Lee and N. R. Armstrong, *J. Phys. Chem. B*, 2003, **107**, 11690.
59 H. Moreira, J. Grisolia, J. Sangeetha, N. M. Decorde, N. Farcau, B. Viallet, K. Chen, G. Viau and L. Ressier, *Nanotechnology*, 2013, **24**, 095701.

 

60 Z.-H. Lin, G. Zhu, Y. S. Zhou, Y. Yang, P. Bai, J. Chen and Z.-L. Wang, *Angew. Chem.*, 2013, **125**, 5169.
61 Y. Min, M. Akbulut, K. Kristiansen, Y. Golan and J. Israelachvili, *Nat. Mater.*, 2008, **7**, 527.
62 G. A. Rance, D. H. Marsh, S. J. Bourne, T. J. Reade and A. N. Khlobystov, *ACS Nano*, 2010, **4**, 4920.
63 I. Horcas, R. Fernandez, J. M. Gomez-Rodriguez, J. M. Colchero, J. Gomez-Herrero and A. M. Baro, *Rev. Sci. Instrum.*, 2007, **78**, 013705.
64 J. M. Soler, E. Artacho, J. D. Gale, A. Garcia, J. Junquera, P. Ordejon and D. Sanchez-Portal, *J. Phys.: Condens. Matter*, 2002, **14**, 2745.